Magnetic and Electric Field Dependent Charge Transfer in Perovskite/Graphene Field Effect Transistors

Nathan D. Cottam, Jonathan S. Austin, Chengxi Zhang, Amalia Patanè, Walter Escoffier, Michel Goiran, Mathieu Pierre, Camilla Coletti, Vaidotas Mišeikis, Lyudmila Turyanska,* and Oleg Makarovsky*

Stable all-inorganic $CsPbX_3$ perovskite nanocrystals (PNCs) with high optical yield can be used in combination with graphene as photon sensors with high responsivity (up to 10^6 A W^{-1}) in the VIS-UV range. The performance of these perovskite/graphene field effect transistors (FET) is mediated by charge transfer processes at the perovskite – graphene interface. Here, the effects of high electric (up to 3000 kV cm^{-1}) and magnetic (up to 60 T) fields applied perpendicular to the graphene plane on the charge transfer are reported. The authors demonstrate electric- and magnetic-field dependent charge transfer and a slow (>100 s) charge dynamics. Magneto-transport experiments in constant (≈ 0.005 T s^{-1}) and pulsed (≈ 1000 T s^{-1}) magnetic fields reveal pronounced hysteresis effects in the transfer characteristics of the FET. A magnetic time is used to explain and model differences in device behavior under fast (pulsed) and slowly (continuous) changing magnetic fields. The understanding of the dynamics of the charge transfer in perovskite/graphene heterostructures developed here is relevant for exploitation of these hybrid systems in electronics and optoelectronics, including ultrasensitive photon detectors and FETs for metrology.

1. Introduction

All-inorganic lead halide perovskites are emerging materials for optoelectronic applications, such as solar cells[1–4] and photodetectors.[5–7] In particular, inorganic halide perovskite nanocrystals (PNCs) have attracted significant attention owing to their unique and outstanding optical properties such as high quantum yield (QY), strong absorption, and widely tunable band gap energy[8–10] accompanied by inexpensive solution processing techniques.[11–13] These PNCs have been successfully used in photon detectors operational in the visible wavelength range with photoresponsivity, $R > 10^5$ A W^{-1},[14,15] and could offer further opportunities for UV applications.[16,17]

Amongst device structures of particular interest are hybrid field effect transistors (FETs) that combine single-layer graphene (SLG) with PNCs. The performance of these devices, such as their response time, is affected by the slow, >1 s, redistribution of charge between the graphene layer and PNCs under light and/or electrostatic gating,[18,19] leading to the accumulation of a large amount of charge in the PNCs (7×10^{12} cm^{-2}[19]). This phenomenon can induce a range of interesting physical phenomena, such as an optically induced Stark effect,[20] large hysteresis on the gate voltage dependence of the graphene resistance,[19] and enhancement of the photoresponsivity.[21,22] However, to fully exploit the potential of perovskite/graphene structures, a comprehensive understanding of their properties is still needed. High magnetic fields are invaluable for interrogating fundamental physical processes

N. D. Cottam, A. Patanè, O. Makarovsky
School of Physics and Astronomy
University of Nottingham
University Park, Nottingham NG7 2RD, United Kingdom
E-mail: Oleg.Makarovsky@nottingham.ac.uk

J. S. Austin, L. Turyanska
Centre for Additive Manufacturing
Faculty of Engineering
University of Nottingham
Jubilee Campus, Nottingham NG8 1BB, United Kingdom
E-mail: Lyudmila.Turyanska@nottingham.ac.uk

The ORCID identification number(s) for the author(s) of this article can be found under https://doi.org/10.1002/aelm.202200995.

C. Zhang
Key Laboratory of Advanced Display and System Applications
Shanghai University
149 Yanchang Road, Shanghai 200072, China

W. Escoffier, M. Goiran, M. Pierre
INSA Toulouse
Université Paul Sabatier
Université de Toulouse
LNCMI UPR CNRS 3228, EMFL, 143 Avenue de Rangueil, Toulouse 31400, France

C. Coletti, V. Mišeikis
Center for Nanotechnology Innovation @NEST
Istituto Italiano di Tecnologia
Piazza San Silvestro, 12, Pisa I-56127, Italy

in low-dimensional materials.[23,24] A complex excitonic structure was uncovered in perovskites and individual excitonic transitions were probed in a magnetic field of up to 60 T.[25,26] Meanwhile, charge transport studies in high magnetic fields revealed unique quantum phenomena in graphene, such as a room temperature quantum Hall effect[24] and a giant quantum Hall effect plateau.[27] To date, the properties of perovskite-graphene heterostructures in high magnetic fields remain largely unknown and could enable a fundamental understanding of the complicated charge transfer mechanisms observed in this system,[19,20] hence advancing their applications.

Here, we investigate graphene devices decorated with a layer of blue-light emitting inorganic cesium lead halide PNCs ($CsPb(Br/Cl)_3$) and study the effects of light, temperature, high electric and magnetic fields (up to 60 T) on the charge dynamics in these heterostructures. We demonstrate the potential of these structures for ultrasensitive VIS-UV photon detectors and uncover complex charge dynamics in these heterostructures.

2. Results

2.1. Perovskite-Graphene Heterostructures

The PNCs have cubic shape and an average size of 16 ± 3 nm (**Figure 1**a and Figure S1, Supporting Information). Their photoluminescence emission is centered at 466 nm with a narrow full width at half maximum (FWHM) of 16 nm (Figure S1, Supporting Information). Size distribution and chemical composition of the PNCs were confirmed by transmission electron microscopy (TEM) and energy dispersive X-Ray (EDX) analysis (Supporting Information SI1 and Figure S2, Supporting Information). The PNCs were used to functionalize CVD-grown graphene using a drop-casting technique. The single-layer graphene was fabricated on a SiO_2/Si substrate with SiO_2 dielectric thickness of 285 nm and processed via electron beam lithography (EBL) into Hall bar geometries (Figure 1b,c).

The gate voltage (V_g) dependence of the resistivity (ρ) for lightly doped n-type pristine graphene (Sample 1) reveals a charge neutrality (Dirac) point at $V_g = -5$ V (Figure 1d), an electron carrier concentration of 3.6×10^{11} cm^{-2} at $V_g = 0$ V, and electron and hole mobilities at room temperature of $\mu_e = 7600$ and $\mu_h = 6500$ cm^2 V^{-1} s^{-1}, respectively. Deposition of the PNCs leads to an increase of the charge mobility to $\mu_e = 14300$ and $\mu_h = 9200$ cm^2 V^{-1} s^{-1}, and a hysteresis of the charge neutrality point between the forward (from negative to positive) and reverse (from positive to negative) sweeps of the gate voltage (Figure 1d). The amplitude of the hysteresis increases monotonously with increasing the sweep voltage range: For sweeps of V_g over a range of 50 V, the charge neutrality point shifts from +5 V to −40 V. A similar behavior is observed in lightly doped p-type graphene (Sample 2) with a Dirac point at $V_g = +15$ V (Figure 1d). Thus, the deposition of the PNCs leads to n-type doping of graphene and a giant hysteresis in ρ (V_g) for both
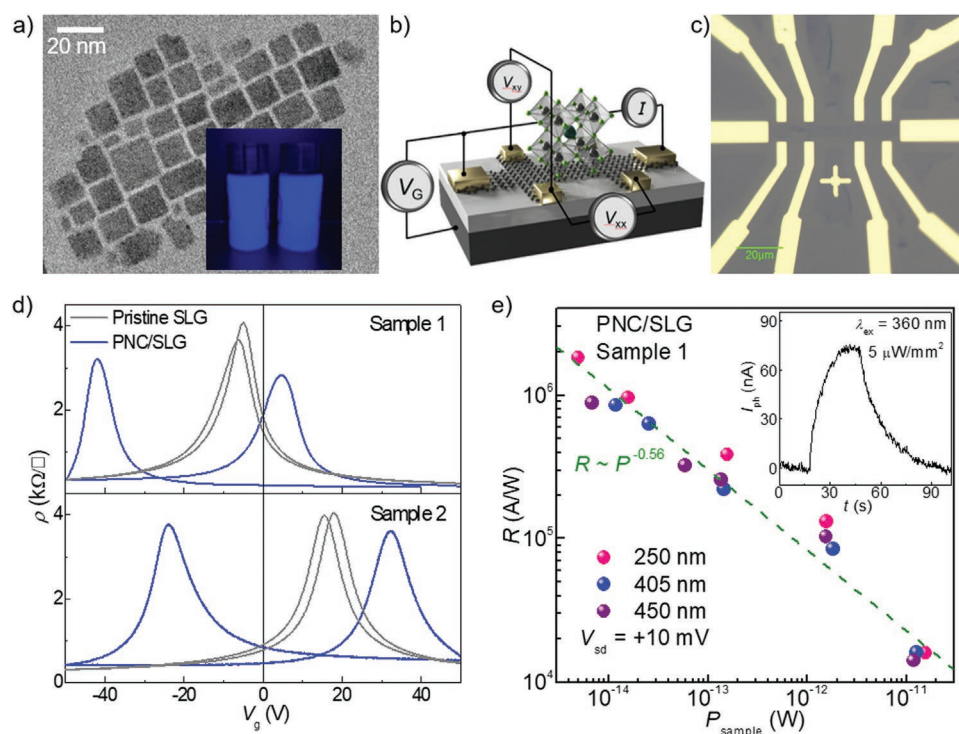

Figure 1. a) Representative transmission electron microscopy (TEM) image of $CsPb(Br/Cl)_3$ nanocrystals and (inset) a photograph of the PNC solutions under UV illumination. b) A schematic and c) an optical image of the graphene/$CsPb(Br/Cl)_3$ Hall bar device. d) Dependence of the resistivity on applied gate voltage, V_g, for two representative devices. Deposition of the PNCs leads to n-type doping and a giant hysteresis in the resistivity-V_g curve, ρ (V_g), independent of the initial pristine graphene properties. e) Responsivity of Sample 1 versus optical power, P_{sample}, under excitation with 250 nm, 405 nm, and 450 nm ($V_{sd} = 10$ mV and $T = 300$ K). Inset shows a typical temporal response of the photocurrent under excitation with 360 nm ($V_{sd} = 10$ mV and $T = 300$ K).
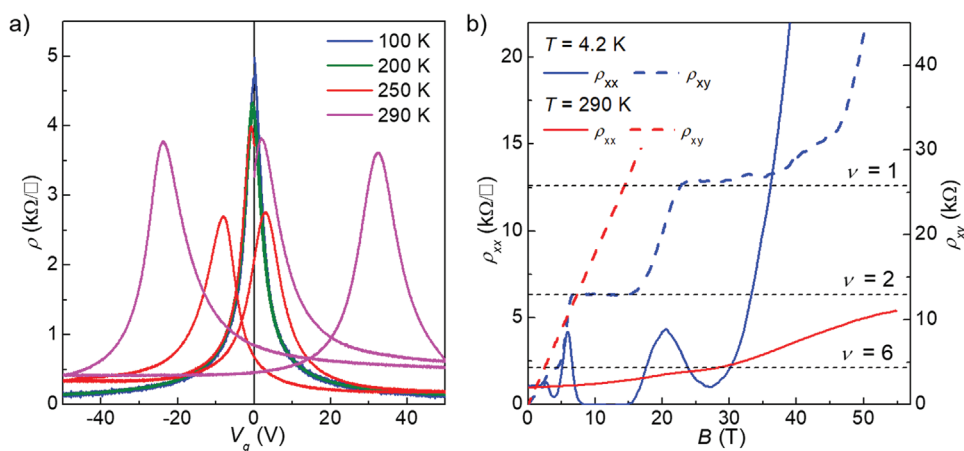
Figure 2. a) Resistivity of the PNC/graphene (Sample 2) measured in the dark using gate voltage sweeps -50 V < V_g < +50 V at 0.1 V s⁻¹ rate at different temperatures. b) Longitudinal (solid lines), ρ_{xx}, and transverse (dashed lines), ρ_{xy}, magnetoresistance at zero gate voltage, $V_g = 0$, $T = 4.2$ K (blue), and 290 K (red). Dashed black lines show positions of the QHE plateau with Landau index $\nu = 1$, 2, and 6.

n- and p-type CVD graphene on conventional Si/SiO$_2$ substrates. This behavior is similar to that reported for CsPbI$_3$/graphene devices and was attributed to the slow transfer of charge between the PNCs and the graphene layer.[19] In the first part of the sweep of V_g to positive gate voltages, negative charges are accumulated in the PNCs by capture of electrons from the graphene layer. During the reverse sweep, holes drift toward the interface and compensate the charges on the PNCs. Thus, the charged PNCs act as effective local gates for graphene. Charges can also be created in the PNCs by optical absorption and can contribute to an enhancement of the photoresponsivity of graphene via charge transfer. We propose that the charging of NC surface defects, such as Pb-related deep traps (activation energy of ≈0.3 eV)[19] is responsible for the observed hysteresis of electrical properties, similar to the results reported for PbS QD decorated graphene.[30] In surface decorated graphene photosensors, the response time and photoresponsivity are defined by the lifetimes of trapped photoexcited charges.[30,31,32] Indeed our devices are photosensitive in the absorption wavelength range of the PNCs and have high photoresponsivity $R > 10^6$ A W⁻¹ in the UV range from 250 to 405 nm (Figure 1e). These high values of the responsivity are comparable to those observed for perovskite/graphene detectors operational in the visible wavelength range.[19,28] The high values of R arise from a large photogain due to the long (seconds) lifetime of the photoexcited charges in PNCs and short (nanoseconds) transport time of electrons in graphene.[18,19,29] The shift of the Dirac point after deposition of PNCs is due to the surface doping of the graphene. The high photosensitivity of the PNC/graphene devices is enabled by the presence of charged defects in the NC layer adjacent to the graphene, which acts as a top-gate, and slow charge transfer between the PNCs and graphene layer, as evident from slow photoresponse times of 8 s and 15 s for the light-ON and light-OFF regimes, respectively (inset in Figure 1e).

The hysteresis of electrical properties shown in Figure 1d was observed over a wide range of temperatures. However, with decreasing temperature, the magnitude of the hysteresis tends to decrease until it totally disappears at $T \approx 200$ K

(Figure 2a). At $T < 250$ K, the $\rho(V_g)$ curve of Sample 2 revealed a pronounced maximum at $V_g \approx 0$, which is independent on the direction of the V_g-sweep and is comparable to that observed for pristine graphene devices. The temperature dependence of $\rho(V_g)$ hysteresis has comparable activation energy with that observed for T-dependent photocurrent,[19] suggesting that both effects are defined by the same Pb-related surface defect state. With decreasing temperature, charge trapping/de-trapping is less effective, hence more symmetric $\rho(V_g)$ dependences are observed with smaller hysteresis, as well as weaker photoresponse. This phenomenon is also observed in graphene devices capped by other NCs.[19] In particular, the hysteresis at large V_g and $T > 250$K suggest a slow charge transfer at the PNCs/graphene interface mediated by defects with deep localized states.

2.2. Observation of Quantum Hall Effect

Gate voltage dependences of the longitudinal (ρ_{xx}) and transverse (ρ_{xy}) resistance were measured in an applied perpendicular magnetic field, B, at low and room temperature (Figure 2b). The applied pulsed magnetic field was ramped from zero to 55 T and back within 100 ms with no measurable hysteresis observed in both $\rho_{xx}(B)$ and $\rho_{xy}(B)$ dependences at such a high field sweep rate. At low temperatures, $T = 4.2$ K, we observe well-formed Quantum Hall Effect (QHE) plateaus of ρ_{xy} and corresponding minima of ρ_{xx} corresponding to Landau indexes $\nu = 1$, 2, and 6 (Figure 2b), similar to that previously reported for exfoliated[23,24] and high-quality CVD graphene[33,34] devices. We note, that both applied V_g and T affect the observation of QHE and the position of the QHE plateau (Supporting Information SI2). Electrical gating changes carrier concentration and, thus, the magnetic field position of the QHE plateau in the transverse magnetoresistance $R_{xy}(B)$ and can even change its polarity. With increasing T, the QHE plateaus are less pronounced, while at $T > 200$ K the QHE is not observed and an almost linear classic Hall effect is observed for $\rho_{xy}(B)$ accompanied by a monotonous $\sim B^2$ increase of ρ_{xx} with weak Shubnikov–de Haas oscillations (Figure 2b).
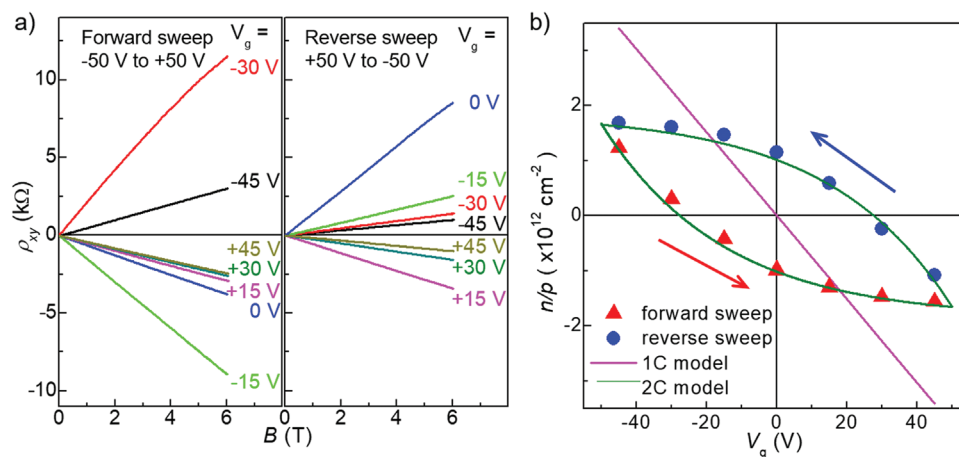
Figure 3. a) Pulsed measurements of $\rho_{xy}(B)$ for Sample 2 acquired during uninterrupted V_g forward sweep (V_g changing from -50 V to $+50$ V, left) and V_g reverse sweep (V_g changing from $+50$ V to -50 V, right) with sweep rate 0.1 V s^{-1} and $T = 290$ K. The value of V_g is indicated for each $\rho_{xy}(B)$ curve. Positive ρ_{xy} corresponds to electron conductivity and negative ρ_{xy} to hole conductivity of graphene. ρ_{xy} measurements taken at the same V_g have the same colour in forward and reverse sweep of V_g. b) Data points – Hall carrier concentration calculated using the ρ_{xy} data presented in (a). Arrows indicate forward (red) and reverse (blue) direction of the V_g sweep. Solid lines represent the calculated dependence of the carrier density n on V_g using two models: conventional 1C model and 2C model with $\tau_{el} = 350$ s, as discussed in the text.

Since the deposition of the perovskite NCs resulted in significant surface doping, we hypothesized that QHE could be observed at higher temperatures, and hence quantum phenomena could affect the charge transfer observed in these devices. However, there is no significant contribution of the perovskite layer to the QHE observed in these devices at high-pulsed (fast-changing) magnetic fields. This is a surprising result as in similar graphene-based systems, such as SiC/graphene and InSe/graphene,[27,35] the $\nu = 2$ quantum Hall plateau becomes extended (>50 T wide). These examples of "giant" quantum Hall effect plateaux in graphene have been assigned to the magnetic field and electric field-induced transfer of charge carriers between the degenerate Landau levels of graphene and localized states in its proximity. We ascribe the absence of a giant QHE plateau in our devices to the fast sweep rate in the pulsed high field ($B < 60$ T) measurements. The time for sweeping the magnetic field (≈ 0.1 s, see Experimental Method) is much shorter than the characteristic "magnetic" time, τ_{mag}, (discussed later in the paper) defined as the time required for charge carriers to be transferred from/into the graphene layer during the increase of the applied magnetic field. This charge transfer process is responsible for the giant QHE $\nu = 2$ plateau in SiC/graphene and InSe/graphene.[35,36] In PNC/graphene systems, τ_{mag} is significantly longer compared to the magnet pulse time of ≈ 0.1 s. The QHE plateau observed in graphene perovskite heterostructures has never been reported before, suggesting that in these devices, the unique quantum properties of graphene can be retained after the deposition of the PNCs and can be complemented by the optical sensitivity of the perovskite layer, enabling fabrication of multifunctional devices.

2.3. Probing Charge Dynamics

We used pulsed magnetic fields to measure ρ_{xy} during uninterrupted cyclic sweeping of the applied gate voltage, i.e., V_g is swept continuously from -50 V to $+50$ V (**Figure 3**a) and ρ_{xy} is measured at a given V_g over a range of magnetic fields. The fast rate of magnetic field sweep of 1000 T s^{-1} and relatively slow gate voltage sweep rate of 0.1 V s^{-1} provide "snapshots" of the graphene transport properties, in particular, the Hall carrier concentration at a constant V_g in the range -50 V $< V_g < +50$ V (symbols in Figure 3b). Data presented in Figure 3 demonstrate that the Hall carrier concentration in graphene can be different at the same value of V_g depending on the direction of the sweep. Thus, the parallel plate capacitor (1C) model commonly used to describe graphene field effect transistors cannot be applied to perovskite functionalized graphene and instead the data is fit by a two-capacitor (2C) model[19] (see Supporting Information SI3). A gate voltage increment ΔV_g generates an incremental increase in the charge ΔQ in the PNCs/graphene heterostructure, which we describe as $\Delta Q = C \Delta V_g$, where ΔQ is the sum of free charge carriers in the single layer graphene (ΔQ_{SLG}) and charges bound onto localized states of the PNCs (ΔQ_{PNCs}), and C is the capacitance of the SiO$_2$ layer. Here, we assume that the charge ΔQ redistributes between the graphene (Q_{SLG}) and the PNCs (Q_{PNCs}) layers with an effective time constant $\tau_{el} = 350$ s. The 2C-model accounts for the dependence of the carrier concentration in graphene on the direction and the rate of the V_g sweep (continuous lines in Figure 3b).

The 2C-model also explains the apparent high field-effect mobility, μ_{FE}, of graphene/perovskite devices at specific V_g sweep conditions presented in **Figure 4**a. By reducing the maximum applied gate voltage to 20 V, we achieve a narrow $\rho_{xx}(V_g)$ peak for the forward sweep of V_g (red curve in inset of Figure 4a). This corresponds to a hole field-effect mobility $\mu_{FE} = 83\,000$ cm^2 V^{-1} s^{-1}, as estimated from the linear fit of the conductivity-V_g curve, $\sigma(V_g)$, shown in the inset of Figure 4a. Note that the hole field-effect mobility calculated in the reverse V_g sweep (blue curve in the inset of Figure 4a) is almost seven times lower: $\mu_{FE} = 12\,000$ cm^2 V^{-1} s^{-1}. The

ADVANCED
SCIENCE NEWS
www.advancedsciencenews.com

ADVANCED
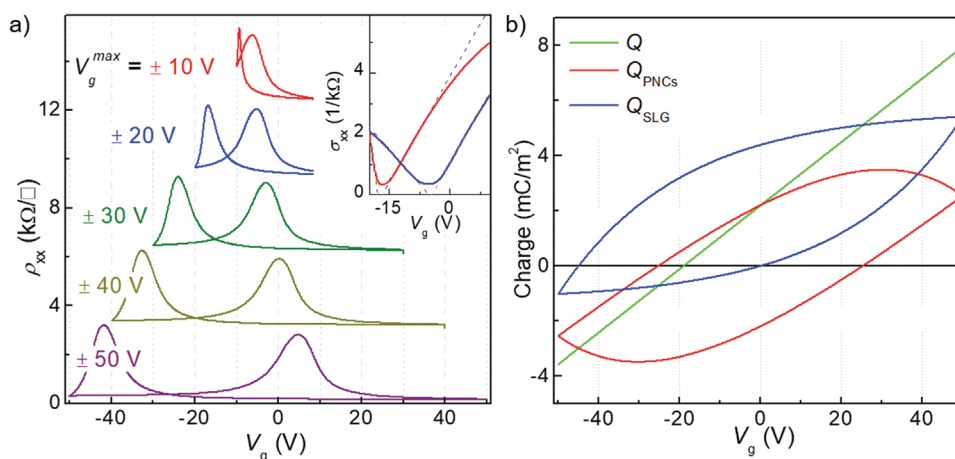**ELECTRONIC**
MATERIALS
www.advelectronicmat.de

Figure 4. a) 2D resistivity of the PNC/graphene Sample 1 for different gate voltage sweeps. Inset: forward (red) and reverse (blue) sweep of conductivity versus gate voltage for sweeps of V_g from -20 V to $+20$ V. Dashed lines show linear fit to the data resulting in hole field effect mobilities of $\mu_{FE} = 83\,000$ cm^2 V^{-1} s^{-1} (forward V_g sweep) and $\mu_{FE} = 12\,000$ cm^2 V^{-1} s^{-1} (reverse V_g sweep). b) Numerical modeling (2C-model) of the total charge Q for the forward and reverse V_g sweeps explained in terms of the charge redistribution between graphene, Q_{SLG}, and the PNCs, Q_{PNCs} (see Supporting Information SI3).

results of the 2C-modeling revealed a hysteresis of the charge distribution between graphene, Q_{SLG}, and the PNCs, Q_{PNCs} for the forward and reverse V_g sweeps (Figure 4b) (see Supporting Information SI3). The observed difference in the measured value of μ_{FE} can be explained by the difference of

the gradient dQ_{SLG}/dV_g at different points of the $Q_{SLG}(V_g)$ hysteretic curve.

The hysteresis in $\rho_{xx}(V_g)$ and the value of the apparent field-effect mobility are influenced by the strength of a continuous applied magnetic field (**Figure 5a**): For $B = 16$ T, the $\rho_{xx}(V_g)$
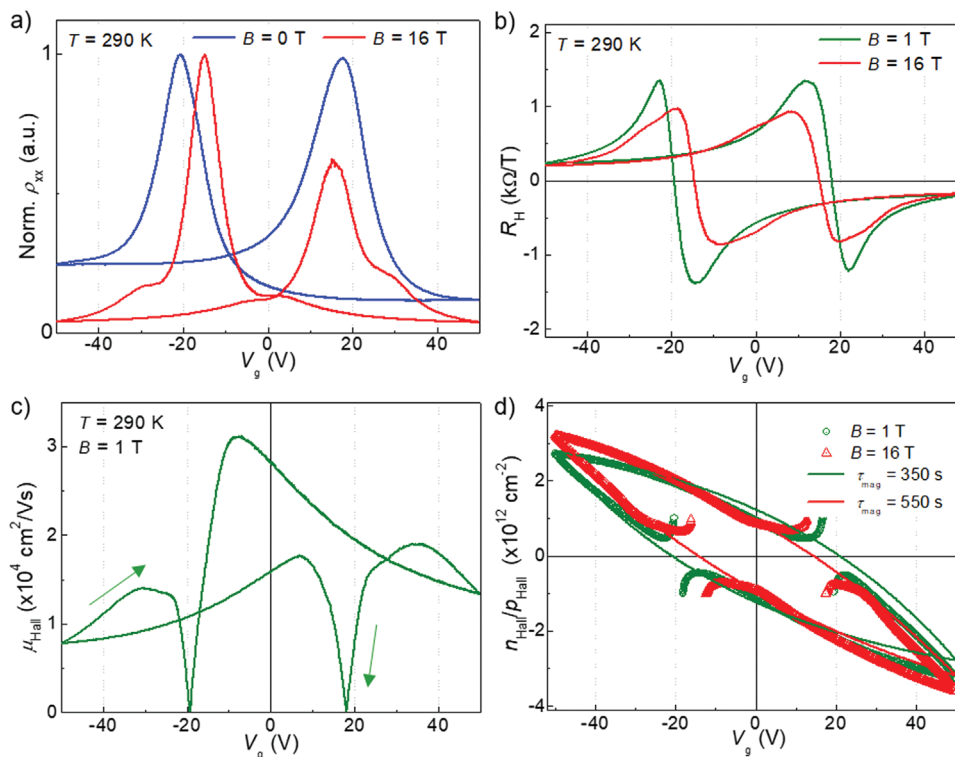

Figure 5. a) Normalised (ρ_{xx}/ρ_{max}) longitudinal resistance as a function of the applied gate voltage for Sample 2 at $B = 0$ T (blue) and 16 T (red) measured during V_g sweep in the range -50 V $< V_g < +50$ V, sweep rate 0.1 V s^{-1}, and $T = 290$ K. b) Hall coefficient R_H as a function of the applied gate voltage at $B = 1$ T (green) and 16T (red) measured during V_g sweep in the range -50 V $< V_g < +50$ V, effective sweep rate 0.15 V s^{-1}, and $T = 290$ K. c) Hall mobility $\mu_{Hall}(V_g)$ calculated from $\rho_{xx}(V_g)$ at $B = 0$ T (blue curve in (a)) and $\rho_{xy}(V_g)$ at $B = 1$ T (green curve in (b)). Arrows indicate the direction of the V_g-sweep. d) Symbols: Hall carrier density $n_{Hall}(V_g)$ at $B = 1$ T (green) and 16 T (red) and corresponding 2C model fits with $\tau_{mag} = 350$ s (green) and $\tau_{mag} = 550$ s (red), respectively.
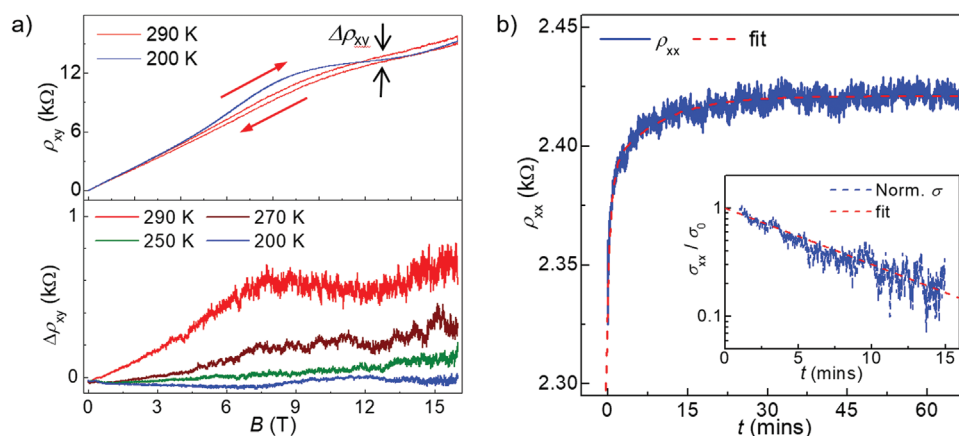
Figure 6. Measurements of Sample 2 in a slow magnetic field. a) Top: transverse magnetoresistance $\rho_{xy}(B)$ at $T = 290$ K (red) and $T = 200$ K (blue), sweep rate ≈0.005 T s^{-1} with 2 h wait at $B = 16$ T field before the downfield sweep. The amplitude of the hysteresis $\Delta\rho_{xy}$ in $\rho_{xy}(B)$ is observed at $T = 290$ K between up and down field sweeps. Bottom: $\Delta\rho_{xy}(B)$ curves measured at different temperatures. b) Time dependence of ρ_{xx} after a magnet quench. The red dashed line is an exponential fit to the data. Inset: log scale fit of the normalized conductivity $\sigma = 1/\rho_{xx}$ by $\sigma \sim \exp(-t/\tau_{mag})$ with $\tau_{mag} = 540$ s.

curve tends to narrow under forward and reverse V_g-sweeps and additional ρ_{xx} peaks emerge at $V_g = \pm 30$ V, which we assign to the Fermi energy (E_F) resonance with the $\nu = 2$ Landau level.[23] Furthermore, the magnitude of the hysteresis tends to weaken in both $\rho_{xx}(V_g)$ and Hall resistance $R_H(V_g)$; in particular, the $R_H(V_g)$ dependences reveal a change of conductivity type at $V_g = \pm 20$ V for the forward and reverse V_g sweeps (Figure 5b).

From the measured $\rho_{xx}(V_g)$ at $B = 0$ and $\rho_{xy}(V_g)$ at $B = 1$ T, we extract the Hall mobility μ_{Hall} (Figure 5c) and Hall carrier concentration n_{Hall} (Figure 5d) under cyclic V_g-sweeps in the range $- 50$ V $< V_g < + 50$ V. The Hall carrier concentration can be fitted by the phenomenological 2C-model (see [19] and Supporting Information SI3) with a characteristic time constant $\tau_{mag} = 350$ s for $B = 1$ T and $\tau_{mag} = 550$ s for $B = 16$ T. The 50% increase of this time at $B = 16$ T indicates that the charge transfer at the PNC/graphene interface tends to be slowed down by a strong magnetic field. This phenomenon can result from the magnetic field-induced localization of the electronic states in graphene and PNCs, thus reducing the cross section for charge transfer. In particular, the magnetic field creates energy gaps near the Dirac point that tend to reduce screening, facilitating the accumulation of localized charge in the proximity of the graphene layer.[37] Interestingly, the measured Hall mobility has a maximum of $\mu_{Hall} = 30\,000$ cm^2 V^{-1} s^{-1} for the forward sweep and $\mu_{Hall} = 20000$ cm^2 V^{-1} s^{-1} for the reverse sweep (Figure 5c). We ascribe the observed 50% increase of the Hall mobility for the forward V_g sweep to the effect of the polarity of charges in PNCs on the carrier scattering time in graphene. For the forward sweep, the charge stored in the PNCs is mostly positive and for the reverse sweep it is negative (Figure 4b). This charge can strongly affect electrostatic potential fluctuations created by the charged impurity centers responsible for the mobility drop in CVD graphene on Si/SiO$_2$ substrates.[38]

To probe further the effect of a magnetic field on the charge transfer, we performed magneto-transport measurements in slow-changing (≈0.005 T s^{-1}) magnetic field sweeps up to $B = 16$ T (**Figure 6**a). For $T > 250$ K, the $\rho_{xx}(B)$ and $\rho_{xy}(B)$ curves reveal hysteresis effects under up and down sweeps of magnetic field. The amplitude of the hysteresis $\Delta\rho_{xy}$ is calculated as the

difference between the values of ρ_{xy} in the up and down sweeps of the magnetic field. From Figure 6a it can be seen that $\Delta\rho_{xy}$ increases linearly with B at low fields and saturates at high fields ($B > 8$ T) corresponding to the QHE plateau with $\nu = 2$. Note that a clear QHE is not observed at $T = 290$ K (Figures 2b, 6a). However, $\Delta\rho_{xy}(B)$ indicates that magnetic-field-dependent charge relaxation in this device is strongly affected by the position of the $\nu = 2$ Landau level even at room temperature.

A fast decrease of the magnetic field from $B = 16$ T to 0 T in a fraction of a second (magnetic field quench) allowed us to estimate the characteristic magnetic relaxation time of the system, $\tau_{mag} = 540$ s (Figure 6b). This time is similar to the time constant $\tau_{mag} = 550$ s previously derived for the hysteresis in $n_{Hall}(V_g)$ in a constant magnetic field $B = 16$ T (Figure 5d). Thus, both electric and magnetic fields influence the charge transfer between the PNCs and graphene. The typical magnetic time constants derived from the analysis of the magneto-transport studies are significantly longer than the characteristic optical times (light-ON and light-OFF times, which have values of 8 s and 15 s, respectively (inset in Figure 1e). In contrast, both τ_{el} and τ_{mag} times in our devices are found to have comparable large values (>100 s). Also, this characteristic time has a magnetic field dependence changing from $\tau_{mag} = \tau_{el} = 350$ s at $B = 0$ T to $\tau_{mag} = 550$ s at $B = 16$ T (Figure 5d). This behavior can be qualitatively explained by additional magnetic-field-induced confinement of charge carriers in graphene, which prevents their transfer to and from the PNCs, thus increasing the effective time constant for the charge transfer and reducing the size of the hysteresis in $\rho_{xx}(V_g)$ and $\rho_{xy}(V_g)$ (Figure 5a,b).

3. Discussion

Our finding of a B-dependent time constant in the PNC/graphene system suggests that a similar time constant should also be measurable in other hybrid heterostructures, such as InSe/graphene[35] and SiC/graphene.[27,39] Despite the significant interest in the SiC/graphene system,[27,36,39,40] to our knowledge, no magnetic time or hysteresis in $\rho_{xy}(B)$ has been reported yet.

**ADVANCED
SCIENCE NEWS**
www.advancedsciencenews.com

**ADVANCED
ELECTRONIC
MATERIALS**
www.advelectronicmat.de

To explain this finding, we suggest that the magnetic time in SiC/graphene is significantly shorter ($\tau_{mag} < 1$ ms) as most of the high field (>50 T) measurements have been conducted using pulsed magnet systems.[39] Such a large difference in the values of τ_{mag} found in different graphene-based systems (>100 s in PNC/graphene and <1 ms in SiC/graphene) could be accounted for by the different properties of the effective barrier for charge transfer between the graphene and adjacent charge-source layer. For SiC/graphene there is virtually no barrier as this material is produced from a single SiC crystal lattice.[36] However, there is a pronounced barrier formed between the PNCs and graphene by the surface ligands in the PNC/graphene system.[12]

The relatively long magnetic time for the PNC/graphene system allowed us to acquire "snapshots" of $\rho_{xy}(B)$ during which the carrier concentration in graphene does not change (Figure 3). This provides accurate Hall carrier concentration and Hall mobility data at any point of the V_g-dependent hysteresis loop. The measurements were also conducted in small ($B = 1$ T) and large ($B = 16$ T) constant magnetic field (Figure 5b–d). For the processing of these data, we assume that $\rho_{xy}(B)$ is a linear function of B (<1 T) at any point of the V_g sweep. Both pulsed (Figure 3b) and constant field (Figure 5d) measurements revealed an "eye-shaped" hysteretic curve for the carrier concentration in graphene $n(V_g)$, which is in agreement with the 2C-model.[19]

The redistribution of carriers between graphene (Q_{SLG}) and PNCs (Q_{PNCs}) can be used to understand the uncertainty of the field-effect mobility, Hall mobility, and large hysteresis of $\rho_{xx}(V_g)$ frequently observed in various graphene FETs functionalized by organic molecules and other charge-trapping layers,[41–43] with the latter effect recently suggested for graphene gas sensors.[44] The field-effect mobility, μ_{FE}, in graphene, is commonly derived using a single parallel plate capacitance model (1C-model) as $\mu_{FE} = \sigma/en$ and $n = V_g C/e$, where σ is conductivity and C is gate capacitance per unit area.[45] Applying this model to our data would lead to μ_{FE} as high as 60 000 cm^2 V^{-1} s^{-1} or as low as 10000 cm^2 V^{-1} s^{-1}, depending on the direction and amplitude of the V_g-sweep (Figure 4a). This uncertainty can be explained using the 2C-model, which demonstrates that $n(V_g)$ has a rather complicated (eye-shaped) dependence on V_g (Figure 4b). Note that μ_{FE} is measured in the region of the maximum $\sigma(V_g)$ slope, which is located in close proximity of the Dirac (charge neutrality) point.[45,46] This point corresponds to the two crossings of the $Q_{SLG}(V_g)$ with $Q = 0$ (blue line in Figure 4b). Positions of these crossings on the "eye-shaped" $Q_{SLG}(V_g)$ curve are defined by the graphene doping level, which shifts the whole curve up or down in the Y (charge) coordinate. Importantly, the curvature of $Q_{SLG}(V_g)$ is different in the different regions of the "eye" curve with the gradient dQ_{SLG}/dV_g much larger in the corners of the eye. Consequently, since $\mu_{FE} = \sigma/Q_{SLG}$, larger dQ_{SLG}/dV_g results in an artificially high μ_{FE}, whereas a smaller dQ_{SLG}/dV_g leads to the opposite effect (Figure 4b). Thus, by changing the V_g sweep rate and V_g maximum, the field effect mobility can be tuned.

Large uncertainty in the mobility measured in structures with significantly slow charge dynamics can be reduced by measurements of the Hall mobility in pulsed (Figure 3) or constant (Figure 5c) magnetic fields. The measured values of the Hall mobility for the forward and reverse sweeps are $\mu_{Hall} = 31\,000$ cm^2 V^{-1} s^{-1} and 20000 cm^2 V^{-1} s^{-1} (Figure 5c). The difference between Hall mobility values is much smaller than the one for the field-effect mobilities of $\mu_{FE} = 60\,000$ cm^2 V^{-1} s^{-1} and 10 000 m^2 V^{-1} s^{-1} (Figure 4a), since Hall carrier concentration provides an accurate direct reading of the $n(V_g)$ dependence. Also, this difference between forward and reverse V_g-sweep Hall mobilities is likely to be relevant to the effect of the impurity charge polarity on the carrier scattering in graphene.

4. Conclusion

We studied stable inorganic perovskites CsPbX$_3$ nanocrystals deposited on high-purity CVD graphene FETs on Si/SiO$_2$ substrates. These devices can be used as photon sensors with high responsivity (up to 10^6 A W^{-1}) in the VIS-UV range. We demonstrated that the performance of these devices is mediated by charge transfer at the PNC/graphene interface and depend on the applied electric field, temperature, and incident light. For the first time, the effect of fast (<100 ms) and slow quantizing magnetic fields on the charge transfer was studied. A characteristic magnetic time was introduced to describe the dependence of the charge transfer on the quantizing magnetic field. A newly developed experimental technique allowed us to study different processes involving charge transfer in this system, such as hysteretic effects in the ρ_{xy} and ρ_{xx} hysteresis, and enhanced field-effect mobility. A phenomenological 2C-model model was successfully applied to explain these phenomena and discuss the prospects and limits of the perovskite/graphene system. Presented findings can improve our understanding of the complicated charge dynamics in functionalized graphene layers and provide novel experimental and theoretical approaches for their studies and improved applications.

5. Experimental Section

Materials: Ultra-clean high-mobility ($\mu \sim 10000$ cm^2 V^{-1} s^{-1} at room temperature) CVD graphene on SiO$_2$/Si substrate (285 nm of SiO$_2$) was produced at the National Enterprise for NanoScience and NanoTechnology (NEST, Italy).[47] Pristine graphene/SiO$_2$/Si wafers were processed into multi-terminal Hall bars and two-terminal diodes. The processing technique can be used to fabricate weakly *n*- and *p*-type graphene field-effect transistors (GFETs) with Dirac point close to zero gate voltage, $|V_g| < 20$ V (Figure 1).

Inorganic CsPb(Br/Cl)$_3$ perovskite nanocrystals were synthesized through a solvothermal method with a mixture of oleic acid (OA), oleylamine (OLA), and didecyldimethylammonium bromide as capping ligands. In a typical process, 0.1 mmol of cesium carbonate, 0.2 mmol of PbBr$_2$, 0.2 mmol of PbCl$_2$, oleic acid (1 mL), oleylamine (1 mL), 0.2 mmol of didecyldimethylammonium bromide and 10 ml hexane were loaded into a Teflon-lined autoclave (50 mL), and then reacted at 160 °C in a muffle furnace for 2.5 h. The crude solution was naturally cooled down to room temperature and purified with ethyl acetate twice. The obtained perovskite nanocrystals were dispersed in 2 mL hexane and centrifuged at 8000 rpm for 2 min to remove large nanocrystals. Graphene devices were functionalized through liquid deposition of perovskite nanocrystals. Following the PNCs deposition, samples were dried in a vacuum ($\approx 10^{-6}$ mbar) overnight.

Morphological, Electrical, and Optical Studies: Transmission electron microscopy (TEM), high-resolution TEM (HRTEM) and were acquired on a JEM-2100F, JOEL operated at 200 kV. Measurements of resistance

and photocurrent were performed using Keithley-2400 SourceMeters and Keithley-2010 multimeters. For photoresponsivity studies, excitation was provided by a UV (250 nm) source and fiber-coupled lasers (405 and 450 nm). The photoresponsivity, R, is defined as photocurrent, I_{pc}, divided by the power of light absorbed by the sample, P_{sample}, where photocurrent is the difference in current, I_{sd}, from the dark state to under illumination.

Studies in Constant and Slow Magnetic Fields B ≤ 16 T: Experimental measurements in constant and slow-changing magnetic fields were performed in a closed-cycle 16 T superconducting solenoid system (Cryogenics Ltd), which includes a cryostat temperature control inset (1.5 K < T < 400 K). For magnetic field-dependent studies, the field sweep rate of ≈0.005 T s^{-1} was used. DC voltage-current dependences were measured using Keithley-2400 SourceMeter units. Cyclic gate voltage, V_g, and sweeps were performed using a constant sweep rate of ≈0.1 V s^{-1}.

Studies in Pulsed Magnetic Fields B ≤ 60 T: Pulsed magnetic field measurements were performed up to $B ≤ 60$ T, field sweep rate ~1000 T s^{-1}. The pulsed magnetic fields are created by discharging a capacitor through a liquid nitrogen-cooled resistive coil in a short time (≈100 ms). The sample was placed in a helium-cooled cryostat and measured in the temperature range 4 K < T < 300 K. A constant DC voltage was applied to a Hall bar sample with either constant applied V_g or cyclic V_g sweeps. The values of longitudinal and transverse voltages were amplified by Stanford SR560 low noise amplifiers and measured using a fast multichannel PXI acquisition card (National Instruments). Parasitic voltages generated during the fast changes of the field were compensated using analysis of the data obtained during field-up and field-down branches of the magnetic pulse.

Supporting Information

Supporting Information is available from the Wiley Online Library or from the author.

Conflict of Interest

The authors declare no conflict of interest.

Author Contributions

N.C., O.M., W.E., M.G, and M.P. performed measurements in magnetic fields. C.C. and V.M. provided pristine graphene and processed it into GFET devices. C.Z., J.A., L.T., and N.C worked on synthesis and characterization of the NCs, and studies of GFETs. O.M., L.T., and N.C developed the used model and applied it to the data. All co-authors contributed to data analysis and interpretation and co-wrote the manuscript.

Data Availability Statement

The data that support the findings of this study are available from the corresponding author upon reasonable request.

[1] J. Wang, J. Zhang, Y. Zhou, H. Liu, Q. Xue, X. Li, C. C. Chueh, H. L. Yip, Z. Zhu, A. K. Y. Jen, *Nat. Commun.* **2020**, *11*, 177.

[2] Y. Pan, Y. Zhang, W. Kang, N. Deng, Z. Yan, W. Sun, X. Kang, J. Ni, *Mater. Adv.* **2022**, *3*, 4053.

[3] Q. Chen, W. Guo, J. C. R. Ke, M. Z. Mokhtar, D. Wang, J. Jacobs, A. G. Thomas, R. J. Curry, Z. Liu, *Sol. RRL* **2021**, *5*, 2000562.

[4] J. Tian, Q. Xue, Q. Yao, N. Li, C. J. Brabec, H.-L. Yip, J. Tian, Q. Xue, Q. Yao, H. Yip, N. Li, C. J. Brabec, *Adv. Energy Mater.* **2020**, *10*, 2000183.

[5] Y. Li, Z. F. Shi, S. Li, L. Z. Lei, H. F. Ji, D. Wu, T. T. Xu, Y. T. Tian, X. J. Li, *J. Mater. Chem. C Mater.* **2017**, *5*, 8355.

[6] C. Bao, J. Yang, S. Bai, W. Xu, Z. Yan, Q. Xu, J. Liu, W. Zhang, F. Gao, C. Bao, W. Zhang, J. Yang, S. Bai, W. Xu, Z. Yan, F. Gao, Q. Xu, J. Liu, *Adv. Mater.* **2018**, *30*, 1803422.

[7] H.-P. Wang, S. Li, X. Liu, Z. Shi, X. Fang, J.-H. He, H. Wang, J. He, S. Y. Li, X. Y. Liu, X. S. Fang, Z. F. Shi, *Adv. Mater.* **2021**, *33*, 2003309.

[8] L. Protesescu, S. Yakunin, M. I. Bodnarchuk, F. Krieg, R. Caputo, C. H. Hendon, R. X. Yang, A. Walsh, M. v. Kovalenko, *Nano Lett.* **2015**, *15*, 3692.

[9] M. Dyksik, H. Duim, D. K. Maude, M. Baranowski, M. A. Loi, P. Plochocka, *Sci. Adv.* **2021**, *7*, 904.

[10] H. C. Sansom, G. Longo, A. D. Wright, L. R. V. Buizza, S. Mahesh, B. Wenger, M. Zanella, M. Abdi-Jalebi, M. J. Pitcher, M. S. Dyer, T. D. Manning, R. H. Friend, L. M. Herz, H. J. Snaith, J. B. Claridge, M. J. Rosseinsky, *J. Am. Chem. Soc.* **2021**, *143*, 3983.

[11] X. Chen, L. Peng, K. Huang, Z. Shi, R. Xie, W. Yang, *Nano Res.* **2016**, *9*, 1994.

[12] C. Zhang, L. Turyanska, H. Cao, L. Zhao, M. W. Fay, R. Temperton, J. O'Shea, N. R. Thomas, K. Wang, W. Luan, A. Patanè, *Nanoscale* **2019**, *11*, 13450.

[13] Y. Zhang, D. Kim, J. H. Yun, J. Lim, M. C. Jung, X. Wen, J. Seidel, E. Choi, M. Xiao, T. Qiu, M. Lyu, E. Q. Han, M. Ghasemi, S. Lim, H. J. Snaith, J. S. Yun, L. Wang, *Adv. Funct. Mater.* **2021**, *31*, 2105542.

[14] C. Li, H. Wang, F. Wang, T. Li, M. Xu, H. Wang, Z. Wang, X. Zhan, W. Hu, L. Shen, *Light: Sci. Appl.* **2020**, *9*, 31.

[15] G. Li, Y. Wang, L. Huang, W. Sun, *ACS Appl. Electron. Mater.* **2022**, *4*, 1485.

[16] M. Gao, C. Zhang, L. Lian, J. Guo, Y. Xia, F. Pan, X. Su, J. Zhang, H. Li, D. Zhang, *J. Mater. Chem. C Mater.* **2019**, *7*, 3688.

[17] M. Liu, S. K. Matta, H. Ali-Löytty, A. Matuhina, G. K. Grandhi, K. Lahtonen, S. P. Russo, P. Vivo, *Nano Lett.* **2022**, *22*, 311.

**ADVANCED
SCIENCE NEWS**

www.advancedsciencenews.com

**ADVANCED
ELECTRONIC
MATERIALS**

www.advelectronicmat.de

[18] M. Gong, R. Sakidja, R. Goul, D. Ewing, M. Casper, A. Stramel, A. Elliot, J. Z. Wu, *ACS Nano* **2019**, *13*, 3714.

[19] N. D. Cottam, C. Zhang, L. Turyanska, L. Eaves, Z. Kudrynskyi, E. E. Vdovin, A. Patane, O. Makarovsky, *ACS Appl. Electron. Mater.* **2020**, *2*, 147.

[20] N. D. Cottam, C. Zhang, J. L. Wildman, A. Patanè, L. Turyanska, O. Makarovsky, N. D. Cottam, C. Zhang, A. Patanè, O. Makarovsky, J. L. Wildman, L. Turyanska, *Adv. Opt. Mater.* **2021**, *9*, 2100104.

[21] A. Daraie, A. Fattah, *Opt. Mater.* **2020**, *109*, 110254.

[22] C. Lee, J. Kim, J. Lee, W. Lee, M. Song, K. Y. Baek, J. Shin, J. Nam, J. Lee, K. Kang, T. Lee, *Adv. Opt. Mater.* **2022**, *10*, 2200049.

[23] K. S. Novoselov, A. K. Geim, S. v. Morozov, D. Jiang, M. I. Katsnelson, I. v. Grigorieva, S. v. Dubonos, A. A. Firsov, *Nature* **2005**, *438*, 197.

[24] K. S. Novoselov, Z. Jiang, Y. Zhang, S. v. Morozov, H. L. Stormer, U. Zeitler, J. C. Maan, G. S. Boebinger, P. Kim, A. K. Geim, *Science* **2007**, *315*, 1379.

[25] A. Miyata, A. Mitioglu, P. Plochocka, O. Portugall, J. T.-W. Wang, S. D. Stranks, H. J. Snaith, R. J. Nicholas, *Nat. Phys.* **2015**, *11*, 582.

[26] A. Surrente, M. Baranowski, P. Plochocka, *Appl. Phys. Lett.* **2021**, *118*, 170501.

[27] J. A. Alexander-Webber, J. Huang, D. K. Maude, T. J. B. M. Janssen, A. Tzalenchuk, V. Antonov, T. Yager, S. Lara-Avila, S. Kubatkin, R. Yakimova, R. J. Nicholas, *Sci. Rep.* **2016**, *6*, 30296.

[28] Y. Lee, J. Kwon, E. Hwang, C.-H. Ra, W. Jong Yoo, J.-H. Ahn, J. Hyeok Park, J. Ho Cho, J. H. Park, J. H. Cho, Y. Lee, C. Ra, W. J. Yoo, J. Kwon, E. Hwang, J. Ahn, *Adv. Mater.* **2015**, *27*, 41.

[29] Y. Wang, Y. Zhang, Y. Lu, W. Xu, H. Mu, C. Chen, H. Qiao, J. Song, S. Li, B. Sun, Y.-B. Cheng, Q. Bao, Y. Wang, Y. Lu, W. Xu, H. Mu, C. Chen, H. Qiao, S. Li, B. Sun, Q. Bao, Y. Zhang, J. Song, Y. Cheng, *Adv. Opt. Mater.* **2015**, *3*, 1389.

[30] G. Konstantatos, M. Badioli, L. Gaudreau, J. Osmond, M. Bernechea, F. P. G. de Arquer, F. Gatti, F. H. L. Koppens, *Nat. Nanotechnol.* **2012**, *7*, 363.

[31] V. K. Singh, S. M. Yadav, H. Mishra, R. Kumar, R. S. Tiwari, A. Pandey, A. Srivastava, *ACS Appl. Nano Mater.* **2019**, *2*, 3934.

[32] S. Fu, I. du Fossé, X. Jia, J. Xu, X. Yu, H. Zhang, W. Zheng, S. Krasel, Z. Chen, Z. M. Wang, K. J. Tielrooij, M. Bonn, A. J. Houtepen, H. I. Wang, *Sci. Adv.* **2021**, *7*.

[33] N. Petrone, C. R. Dean, I. Meric, A. M. van der Zande, P. Y. Huang, L. Wang, D. Muller, K. L. Shepard, J. Hone, *Nano Lett.* **2012**, *12*, 2751.

[34] S. Pezzini, V. Mišeikis, S. Pace, F. Rossella, K. Watanabe, T. Taniguchi, C. Coletti, *2D Mater.* **2020**, *7*, 041003.

[35] Z. R. Kudrynskyi, M. A. Bhuiyan, O. Makarovsky, J. D. G. Greener, E. E. Vdovin, Z. D. Kovalyuk, Y. Cao, A. Mishchenko, K. S. Novoselov, P. H. Beton, L. Eaves, A. Patanè, *Phys. Rev. Lett.* **2017**, *119*, 157701.

[36] S. Kopylov, A. Tzalenchuk, S. Kubatkin, V. I. Fal'ko, *Appl. Phys. Lett.* **2010**, *97*, 112109.

[37] S. Slizovskiy, *Phys. Rev. B Condens. Matter Mater. Phys.* **2015**, *92*, 195426.

[38] S. Adam, E. H. Hwang, V. M. Galitski, S. das Sarma, *Proc. Natl. Acad. Sci. U.S.A.* **2007**, *104*, 18392.

[39] M. Yang, O. Couturaud, W. Desrat, C. Consejo, D. Kazazis, R. Yakimova, M. Syväjärvi, M. Goiran, J. Béard, P. Frings, M. Pierre, A. Cresti, W. Escoffier, B. Jouault, *Phys. Rev. Lett.* **2016**, *117*, 237702.

[40] R. Ribeiro-Palau, F. Lafont, J. Brun-Picard, D. Kazazis, A. Michon, F. Cheynis, O. Couturaud, C. Consejo, B. Jouault, W. Poirier, F. Schopfer, *Nat. Nanotechnol.* **2015**, *10*, 965.

[41] D. B. Farmer, G. M. Roksana, V. Perebeinos, Y. M. Lin, G. S. Tuievski, J. C. Tsang, P. Avouris, *Nano Lett.* **2009**, *9*, 388.

[42] H. Wang, Y. Wu, C. Cong, J. Shang, T. Yu, *ACS Nano* **2010**, *4*, 7221.

[43] L. Xu, I.-C. Ni, Y.-P. Chao, T.-J. Jiang, M.-H. Chen, C.-I. Wu, L. Xu, I.-C. Ni, Y.-P. Chao, T.-J. Jiang, C.-I. Wu, M.-H. Chen, *Adv. Mater. Interfaces* **2021**, *8*, 2100748.

[44] J. Gao, C. Wang, Y. Chu, Y. Han, Y. Gao, Y. Wang, C. Wang, H. Liu, L. Han, Y. Zhang, *Talanta* **2022**, *240*, 123197.

[45] S. v. Morozov, K. S. Novoselov, M. I. Katsnelson, F. Schedin, D. C. Elias, J. A. Jaszczak, A. K. Geim, *Phys. Rev. Lett.* **2008**, *100*, 016602.

[46] J. H. Gosling, O. Makarovsky, F. Wang, N. D. Cottam, M. T. Greenaway, A. Patanè, R. D. Wildman, C. J. Tuck, L. Turyanska, T. M. Fromhold, *Commun. Phys.* **2021**, *4*, 30.

[47] A. Tyagi, V. Mišeikis, L. Martini, S. Forti, N. Mishra, Z. M. Gebeyehu, M. A. Giambra, J. Zribi, M. Frégnaux, D. Aureau, M. Romagnoli, F. Beltram, C. Coletti, *Nanoscale* **2022**, *14*, 2167.

2200995 (9 of 9)